ADVANCED MATERIALS INTERFACES

www.advmatinterfaces.de

Ultrastable Lead-Free Double Perovskite Photodetectors with Imaging Capability

Ying Li, Zhifeng Shi, Lingzhi Lei, Sen Li, Dongwen Yang, Di Wu, Tingting Xu, Yongzhi Tian, Yingjie Lu, Ye Wang, Lijun Zhang, Xinjian Li,* Yuantao Zhang, Guotong Du, and Chongxin Shan*

Recently, the halide perovskites have increasingly received attention because of their superior capabilities in photodetector applications. However, the well-known instability and lead-toxicity are two major obstacles for their commercialization and practical applications. In this work, self-powered photodetectors based on solution-processed double perovskite $Cs_2AgBiBr_6$ films are fabricated for the first time. Owing to the high material integrity of $Cs_2AgBiBr_6$ and efficient interfacial charge transfer from perovskite to the underlying electron-quenching layer, the photodetector demonstrates excellent performances. Especially, the unencapsulated device demonstrates a good working stability in the open air. Typically it has the ability to endure a high temperature of 373 K for 10 h continuous running, demonstrating a good temperature resistance. In addition, after 3-month storage in open air, the photodetection capability of the device can almost be maintained. By deploying the photodetector as a point-like sensing pixel, high-resolution imaging patterns are acquired, which is the first report on imaging applications of lead-free perovskite photodetectors. The obtained results suggest that the lead-free double perovskite $Cs_2AgBiBr_6$ is potentially an attractive candidate to be applied in high-efficiency and stable photodetectors that can be employed in optical imaging.

1. Introduction

Photodetectors that can covert incident optical signals to electrical signals are crucial for a wide range of applications including environmental monitoring, medial analysis, security surveillance, optical communications, and biological sensing, etc.[1–3] A good commercialization prospect can be expected for the photodetectors that possess high responsivity, fast response speed, low power consumption, good stability, and low processing cost. Among the various semiconductor materials explored for light detection, the newly emerging organic–inorganic hybrid perovskites ($CH_3NH_3PbX_3$, X = Cl, Br, I) have triggered an increasingly intensive concern. The appealing properties of this new class of materials that might enable advances in photodetectors are their large carrier diffusion length, large light absorption coefficients, high and well-balanced carrier mobility, low exciton binding energy, and the low-temperature material processing technique.[4–11] By employing such materials as the light absorber, many breakthroughs in developing high-performance and low-cost perovskite photodetectors have been witnessed in recent years.[12–19] Despite the stunning progress that has been made on $CH_3NH_3PbX_3$-based photodetectors, the toxicity and environmental instability have cast a gloomy shadow

Dr. Y. Li, Dr. Z. Shi, Dr. D. Yang, Dr. D. Wu, Dr. T. Xu, Dr. Y. Lu, Dr. Y. Wang, Prof. X. Li, Prof. C. Shan
Key Laboratory of Materials Physics of Ministry of Education
Zhengzhou University
Daxue Road 75, Zhengzhou 450052, China
E-mail: shizf@zzu.edu.cn; lixj@zzu.edu.cn

Dr. Y. Li, Dr. Z. Shi, Dr. L. Lei, Dr. S. Li, Dr. D. Wu, Dr. T. Xu, Prof. Y. Tian, Dr. Y. Lu, Dr. Y. Wang, Prof. X. Li, Prof. C. Shan
School of Physics and Engineering
Zhengzhou University
Kexue Road 100, Zhengzhou 450001, China

Prof. L. Zhang
State Key Laboratory of Superhard Materials
Key Laboratory of Automobile Materials of MOE
and Department of Materials Science and Engineering
Jilin University
Changchun 130012, China

The ORCID identification number(s) for the author(s) of this article can be found under https://doi.org/10.1002/admi.201900188.

DOI: 10.1002/admi.201900188

Prof. Y. Zhang, Prof. G. Du
State Key Laboratory on Integrated Optoelectronics
College of Electronic Science and Engineering
Jilin University
Qianjin Street 2699, Changchun 130012, China

Prof. G. Du
School of Physics and Optoelectronic Technology
Dalian University of Technology
Dalian 116023, China

Prof. C. Shan
State Key Laboratory of Luminescence and Applications
Changchun Institute of Optics
Fine Mechanics and Physics
Chinese Academy of Sciences
Changchun 130033, China

over their further applications. Therefore, searching environmentally stable and lead-free perovskites to address the above hurdles is imperative and certainly a worthwhile subject. Currently, numerous theoretical and experimental efforts have been devoted to screen suitable perovskites, and a few promising candidates have been identified. In this context, substitution of Pb^{2+} by homovalent group-14 element Sn^{2+} has become the research focus because both two elements have the similar diameter and electron structure.[20,21] Unfortunately, the thermodynamically favored Sn^{4+} makes oxidation a critical stability drawback for Sn(II)-based perovskites and devices. Recent studies have verified that the simple combinatory of ionic charges in the $A^+B^{2+}X_3$ formula could not lend much hope for screening alternatives to the $CH_3NH_3PbX_3$ with comparable optical and electrical characteristics,[22] and there are few, if any, suitable 2+ cations with a $d^{10}s^0$ or $d^{10}s^2$ configuration that are both environmentally stable and nontoxic. Very recently, a heterovalent substitution concept with a pair of Pb(II) ions replaced by one monovalent B^+ and one trivalent B^{3+} ions to form $A_2B^+B^{3+}X_6$ double perovskites structure,attracts intensive attention.[22–28] To keep long-pair states located at the band edges, the most favorable candidate for B^{3+} is Bi^{3+} or Sb^{3+}, and the most desirable element for B^+ is In^+ or Tl^+.[28,29] However, double perovskite containing In^+ is intrinsically instable and Tl^+ is water-soluble and toxic.[30] Among all of the possible arrangements of $A_2B^+B^{3+}X_6$, $Cs_2AgBiBr_6$ is proposed as one of the promising replacements of the conventional lead halides. Experimentally, solution synthesis of the $Cs_2AgBiBr_6$ single crystals and quantum dots has been reported in Tang's and Han's groups,[31,32] exhibiting many appealing features of high defect tolerance, good material stability, and long carrier recombination lifetime. Besides, solar cells and photocatalytic applications based on the double perovskites $Cs_2AgBiBr_6$ have been successfully demonstrated.[33,34] However, the application of such materials in photodetectors is rarely reported as far as we know. Moreover, in previous studies on perovskite-based photodetectors, the device performance in terms of photoresponsivity, on/off photocurrent ratio, specific detectivity, and other related parameters has always been highlighted, but crucial stability studies on the unencapsulated device have been rarely reported. To be employed more widely in photodetection fields, investigation on the operation stability of perovskite-based photodetectors is highly desired and necessary to be promoted.

In this work, for the first time, we demonstrated a self-powered perovskite photodetector by employing solution-processed lead-free double perovskite $Cs_2AgBiBr_6$ films as the light absorber. Owing to the high material integrity of $Cs_2AgBiBr_6$ and efficient interfacial charge transfer from perovskite to the underlying electron-quenching layer, an excellent photodetection performance was achieved. More importantly, the unencapsulated photodetector demonstrates a remarkable operation stability against water and oxygen degradation (air ambient, 35–50% humidity). Even at a high working temperature of 373 K for 10 h continuous running or after storage in open air for three months, the photodetection ability can be efficiently sustained, indicating a good temperature resistance and a desired compatibility for practical applications. Further, the photodetector was employed as the sensing pixels in an imaging system, and high-resolution imaging patterns were obtained. The obtained results demonstrate that the lead-free double perovskites $Cs_2AgBiBr_6$ is an attractive candidate for the fabrication of environment-friendly and high-performance photodetectors that can be employed in imaging.

2. Results and Discussion

Figure 1a presents the typical scanning electron microscope (SEM) images of the as-grown $Cs_2AgBiBr_6$ films on the n-type GaN template, which displays a smooth and dense morphology with a high surface coverage. One can see that the $Cs_2AgBiBr_6$ films obtained are composed of large particles with their grain size distributing in a range of 200–400 nm. Unlike other reports, no pinholes or impurities can be observed from the SEM image, indicating a good crystallinity of the resulting perovskite products and favoring an improved electrical transport ability. Additionally, the atom force microscopy (AFM) image was also tested. The films are composed of dense particles with a grain size distribution in a range of 200–400 nm, which is consistent with the SEM result. The corresponding surface roughness is about 9.72 nm (Figure S1, Supporting Information). The inset of Figure 1a presents the cross-sectional SEM image of the $Cs_2AgBiBr_6$/GaN heterostructure, from which the densely packed sub-micrometer–sized grains and uniform hetero-interface can be identified. Note that such a morphology feature is beneficial for the performance of photovoltaic photodetectors because there is no grain boundary in the vertical direction of $Cs_2AgBiBr_6$ grain, which is of crucial importance for the efficient carrier transfer in photodetectors. Besides, the thickness of the $Cs_2AgBiBr_6$ films was estimated to be ≈250 nm from the cross-sectional SEM image. By using the energy dispersive X-ray spectroscopy (EDS) measurements, the elemental composition and distribution in $Cs_2AgBiBr_6$ films were also investigated. As shown in Figure 1b, the Cs, Ag, Bi, and Br elements are uniformly distributed throughout the selected square area in Figure 1a. Quantitative analysis of the EDS spectrum shown in Figure S2 (Supporting Information) gives a quantified atomic ratio (%) of 16.84:9.32:9.83:64.02 (1.81:1:1.05:6.87) for Cs:Ag:Bi:Br, which is close to the stoichiometry of $Cs_2AgBiBr_6$ material. Figure S3 (Supporting Information) displays the total X-ray photoelectron spectrometer (XPS) spectrum of the $Cs_2AgBiBr_6$ films in which the signals associated with four elements were detected. The molar ratio of the incorporated Cs, Ag, Bi, and Br is 1.96:1:1.02:6.29, consistent with the data obtained in EDS measurements shown above. Further, the XPS spectra of Cs 3d, Ag 3d, Bi 4f, and Br 3d of $Cs_2AgBiBr_6$ films were analyzed to investigate the chemical bond configuration of the elements, as displayed in Figure 1c. In addition, X-ray diffraction (XRD) measurements were carried out to examine the structural properties of the $Cs_2AgBiBr_6$ films. As presented in Figure 1d, the peaks at 13.82°, 15.92°, 22.49°, 27.61°, and 31.91° can be assigned to the diffractions from (111), (002), (022), (222), and (004) planes of crystalline cubic $Cs_2AgBiBr_6$. The space group $Fm\bar{3}m$ and the obtained cubic cell unit (a = 11.18 Å) are in good agreement with previous reports.[21,25,32] Note that no other peaks (e.g., AgBr, $Cs_3Ag_2Br_9$) were detected in addition to the characteristic

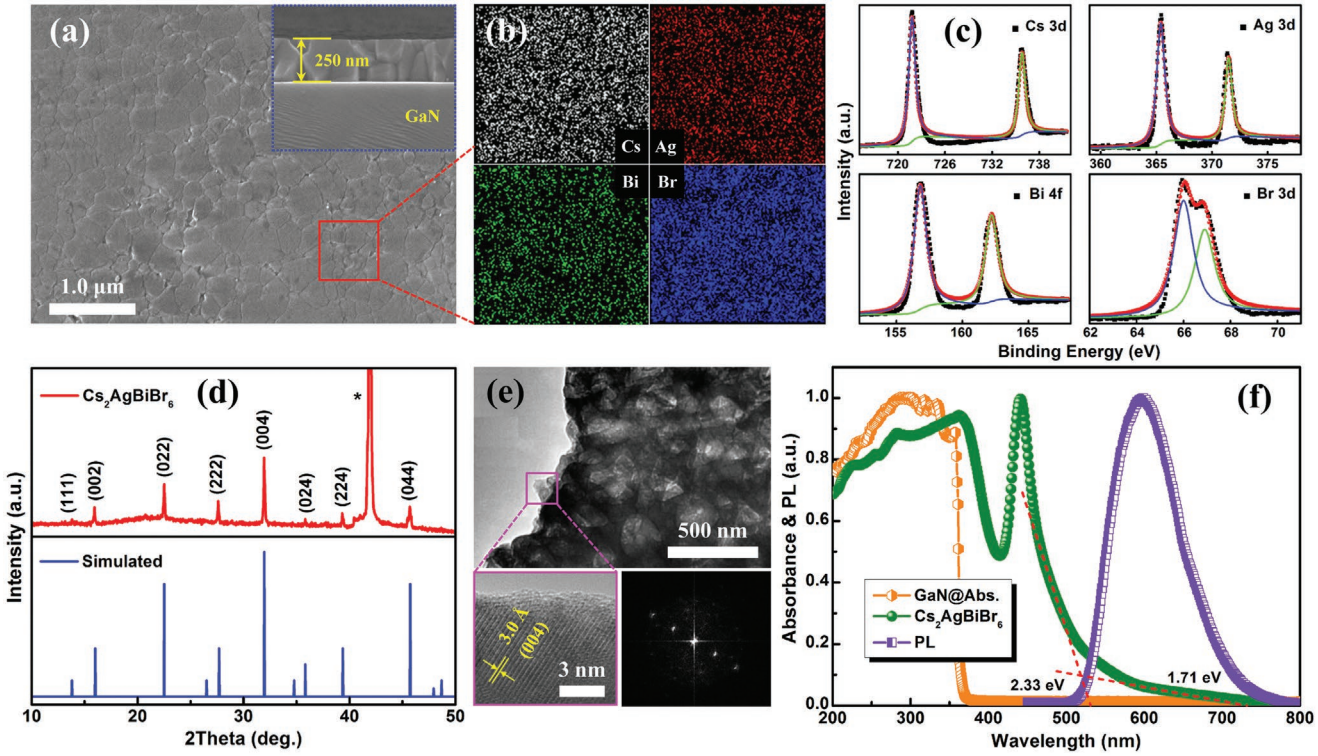

Figure 1. a) Top-view SEM images of the $Cs_2AgBiBr_6$ perovskites films on GaN template. The inset shows the cross-sectional SEM image of the $Cs_2AgBiBr_6$/GaN heterostructure. b) EDS elemental mapping results. c) XPS data corresponding to Cs 3d, Ag 3d, Bi 4f, and Br 3d of the $Cs_2AgBiBr_6$ films. d) XRD patterns (upper) of the as-grown $Cs_2AgBiBr_6$ films and the standard XRD patterns (bottom) for cubic $Cs_2AgBiBr_6$. The asterisk (*) indicates the reflection position of underlying template. e) TEM image of the as-grown $Cs_2AgBiBr_6$ nanograins and the corresponding FFT image. f) Absorption spectra of the $Cs_2AgBiBr_6$ films and GaN layer, and PL spectra of the $Cs_2AgBiBr_6$ films.

diffraction from the sapphire substrate (marked by asterisk (*)), suggesting a high phase purity of cubic double perovskites. The corresponding crystal structures were shown in Figure S4 (Supporting Information), where Ag^+ and Bi^{3+} ions located on the B and B′ sites in the ordered double-perovskite lattice ($A_2BB'X_6$). Ag^+ and Bi^{3+} ions are bonded with Br^- to form $(AgBr_6)^{5-}$ and $(BiBr_6)^{3-}$ octahedron, respectively. These two octahedra alternately link into a rock-salt face-centered cubic structure, with larger Cs^+ filling into their gaps, forming the typical $A_2BB'X_6$ structure. Figure 1e shows the high-resolution transmission electron microscope (TEM) image of the as-grown $Cs_2AgBiBr_6$ nanograins, which were scraped from the bottom template. A set of clear lattice fringes can be identified with an interplanar spacing of ≈0.30 nm, corresponding to the (004) crystal planes of cubic $Cs_2AgBiBr_6$. The corresponding Fourier transformation (FFT) image displayed in right-bottom pane verifies the single-crystalline characteristics of the $Cs_2AgBiBr_6$ nanograins.

The optical properties of the $Cs_2AgBiBr_6$ films were further investigated by using ultraviolet–visible absorption and photoluminescence (PL). As shown in Figure 1f, the absorption onset of the $Cs_2AgBiBr_6$ films locates at about 720 nm, followed by a sharp increase in absorption near 535 nm, which may be due to the indirect allowed transitions involving the phonon-assisted processes. The indirect bandgap feature of $Cs_2AgBiBr_6$ with the valence band maximum (VBM) at X point and the conduction band minimum (CBM) at L point has been confirmed by the electronic band structure calculations shown in Figure S5 (Supporting Information), as is consistent with previous report.[28] From the partial density of states (PDOS) diagram, the VBM consists of antibonding states of Bi 6s and Br p orbitals, and the CBM mainly derives from the Bi 6p states. The indirect bandgap for $Cs_2AgBiBr_6$ results from the angular momentum mismatch of the orbitals that comprise the VBM and CBM. Besides, an obvious absorption peak at about 436 nm could be attributed to the exciton absorption, similar to the observations in previous study.[35] The purple dotted line in Figure 1f presents the PL spectrum of the $Cs_2AgBiBr_6$ films peaking at 2.07 eV, within the range of previously reported results (1.83–2.25 eV), and the relatively large scope of the reported values most likely originates from different synthesis conditions and measurement methods used in the different studies.[36,37] Herein, one point should be noted that the emission intensity is reduced by ≈34% in contact with the GaN template, which implies the charge transfer behavior from the $Cs_2AgBiBr_6$ films to the GaN material, as required for working photovoltaic photodetectors (as discussed later). Besides, the absorption of the GaN layer (yellow dotted line) was also measured, and a sharp absorption edge at ≈365 nm can be observed. The electrical properties of GaN layer are presented in Table S1 (Supporting Information).

As is well known, the stability of halide perovskites has always been criticized, which is the main obstacle significantly hindering their potential applications in optoelectronic devices. By the phase stability diagrams analysis, we first investigate the

thermodynamic stability of $Cs_2AgBiBr_6$ against possible competing phases in theory, including the CsBr, $CsBr_3$, AgBr, $BiBr_3$, BiBr, Cs_3Bi_2, Cs_3Bi, $CsBi_2$, $CsAgBr_2$, $CsAgBr_3$, and Cs_2AgBr_3. As shown in Figure S6 (Supporting Information), the chemical potential window against $\Delta\mu_{Ag}$ and $\Delta\mu_{Cs}$ was determined at fixed chemical potential of Bi in which the sliced polygon region stabilizing the $Cs_2AgBiBr_6$ phase was marked in green and the surrounding lines represent the direct competing phases. It can be seen that the $Cs_2AgBiBr_6$ exhibits a quite large chemical potential window, as compared with the ABX_3 halide perovskites,[38,39] suggesting the easy formation of pure $Cs_2AgBiBr_6$ phase, and also explaining the superior stability for $Cs_2AgBiBr_6$ films as discussed later in a sense. Experimentally, the environmental stability of the as-grown $Cs_2AgBiBr_6$ was assessed by investigating the effects of storage period, ultraviolet (UV) light irradiation, and heat on the structural and optical properties of such lead-free double perovskites. As shown in **Figure 2**a, the as-grown $Cs_2AgBiBr_6$ sample possesses a good chemical stability, which preserves its structural integrity after 40-day storage in ambient conditions (20 °C, 35–50% humidity) without the appearance of other additional diffractions, demonstrating a higher stability against water and oxygen degradation than the organic–inorganic hybrid perovskites.[40,41] Moreover, the initial PL performance of the $Cs_2AgBiBr_6$ films can almost be maintained, as displayed in Figure 2b. Whereas, the emission decay for lead halide perovskite counterparts is very significant even with a shorter 10-day storage (90% decay, Figure S7, Supporting Information), which suggests that the lead-free $Cs_2AgBiBr_6$ films can serve as reliable building blocks for device applications. Further, the photostability test of the $Cs_2AgBiBr_6$ films was implemented under continuous UV light irradiation. Unexpectedly yet interestingly, a PL enhancement behavior was observed over the test period (12.5 h), as shown in Figure 2c, and such "photoactivation" phenomenon has been reported in previous study,[42] which may result from the removal of undesired surface states or dangling bonds by high-energy photons under UV light irradiation. The inset in Figure 2c displays the corresponding PL spectra recorded before and after photostability test; except for a substantial increase in PL intensity, the peak position and linewidth of the PL spectra are almost unchanged. Further, the successive heating/cooling cycling measurements of the $Cs_2AgBiBr_6$ films were performed in the temperature range of 293–373 K, and the integrated PL intensity at all temperature points were plotted in Figure 2d–f. It can be seen that the relative PL intensity decreases gradually with the increasing temperature owing to the fluorescence quenching (heating process, cycle 1), and a small emission decay of about 12.5% was produced after the first cooling process. The unrecoverable behavior of the PL performance may be related to the added structural defects in the $Cs_2AgBiBr_6$ films caused by the heating effect; thus, the radiative recombination probability of photo-generated carriers was reduced accordingly. Another observation is that the attenuation of PL intensity is slightly reduced after cycles 2 and 3 cooling processes. After three successive heating/cooling cycling tests, the PL intensity exhibits 18.2% decay altogether. Even after

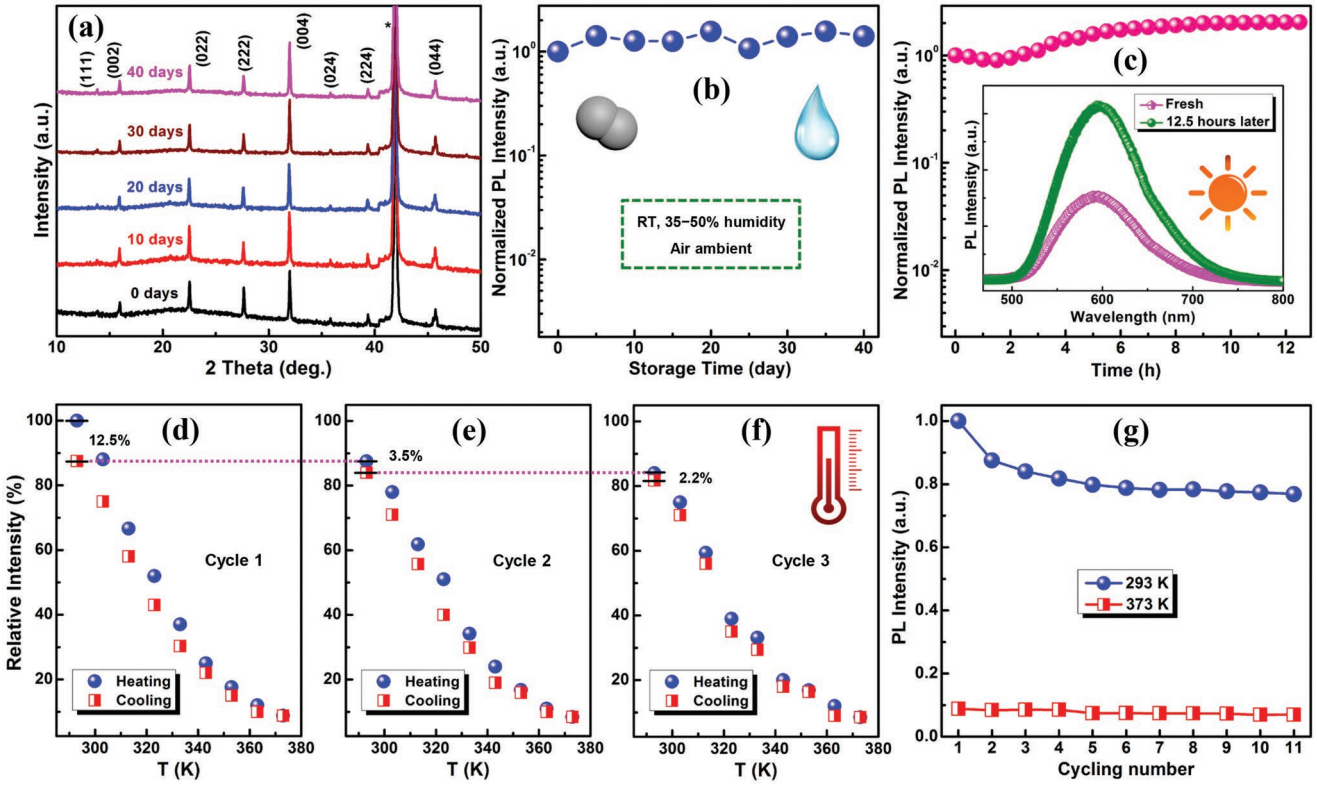

Figure 2. a) XRD patterns, b) PL intensity evolution of the $Cs_2AgBiBr_6$ films after different storage periods. c) Photostability test of the as-grown $Cs_2AgBiBr_6$ films under continuous UV light irradiation (365 nm, 3.0 mW). d–f) Three heating/cooling cycling measurements of the $Cs_2AgBiBr_6$ films. g) Integrated PL intensity of the $Cs_2AgBiBr_6$ films at two representative temperature points (293 and 373 K) over eleven cycling measurements.

eleven measurement cycles, ≈77% of the original emission intensity has been retained, as summarized in Figure 2g with two representative temperature points (293 and 373 K). The above results indicate a remarkable stability of the $Cs_2AgBiBr_6$ films against environment oxygen/moisture, light and heat, and are also evident of the reliable $Cs_2AgBiBr_6$ light absorber compatible for practical applications under harsh conditions.

Figure 3a depicts the schematic structure and photograph of the $Cs_2AgBiBr_6$/GaN heterojunction photodetector. This special structural configuration is characterized by the formation of a built-in electrical field at the hetero-interface by which the device is capable of separating the photogenerated electron–hole pairs in an efficient way. The detailed photoresponse behaviors of the $Cs_2AgBiBr_6$/GaN heterojunction photodetector can be well understood from the energy band profile of the planar heterojunction, as illustrated in the right-bottom pane of Figure 3a. In present case, the conduction band minimum and valence band maximum of $Cs_2AgBiBr_6$ layer are −3.79 and −6.04 eV, respectively, and those of GaN are −4.1 and −7.5 eV. Owing to the desired staggered band alignment, the electrons will transfer from the $Cs_2AgBiBr_6$ layer to the GaN, and holes move in the opposite direction after two semiconductor materials contact. Thus, the energy levels near the $Cs_2AgBiBr_6$ surface will bend downward while the energy levels near the GaN surface will bend upward. As a result, a built-in electric field will appear near the $Cs_2AgBiBr_6$/GaN interface. Under illumination, absorption of the incident light will result in the generation of electron–hole pairs, which will be rapidly separated by the built-in electric field and then transferred to the electrodes to produce photocurrent. Moreover, the electron transfer from the $Cs_2AgBiBr_6$ to GaN would elevate (lower) the Fermi level of GaN ($Cs_2AgBiBr_6$) and thus reduce the contact barrier, leading to a rapid carriers extraction and also a high photocurrent. As a result, the interfacial charge transfer caused by the built-in electric field not only inhibits the undesirable charge recombination but also lowers the barrier height, and a fast response and a high responsivity can be expected for the proposed heterojunction photodetector.

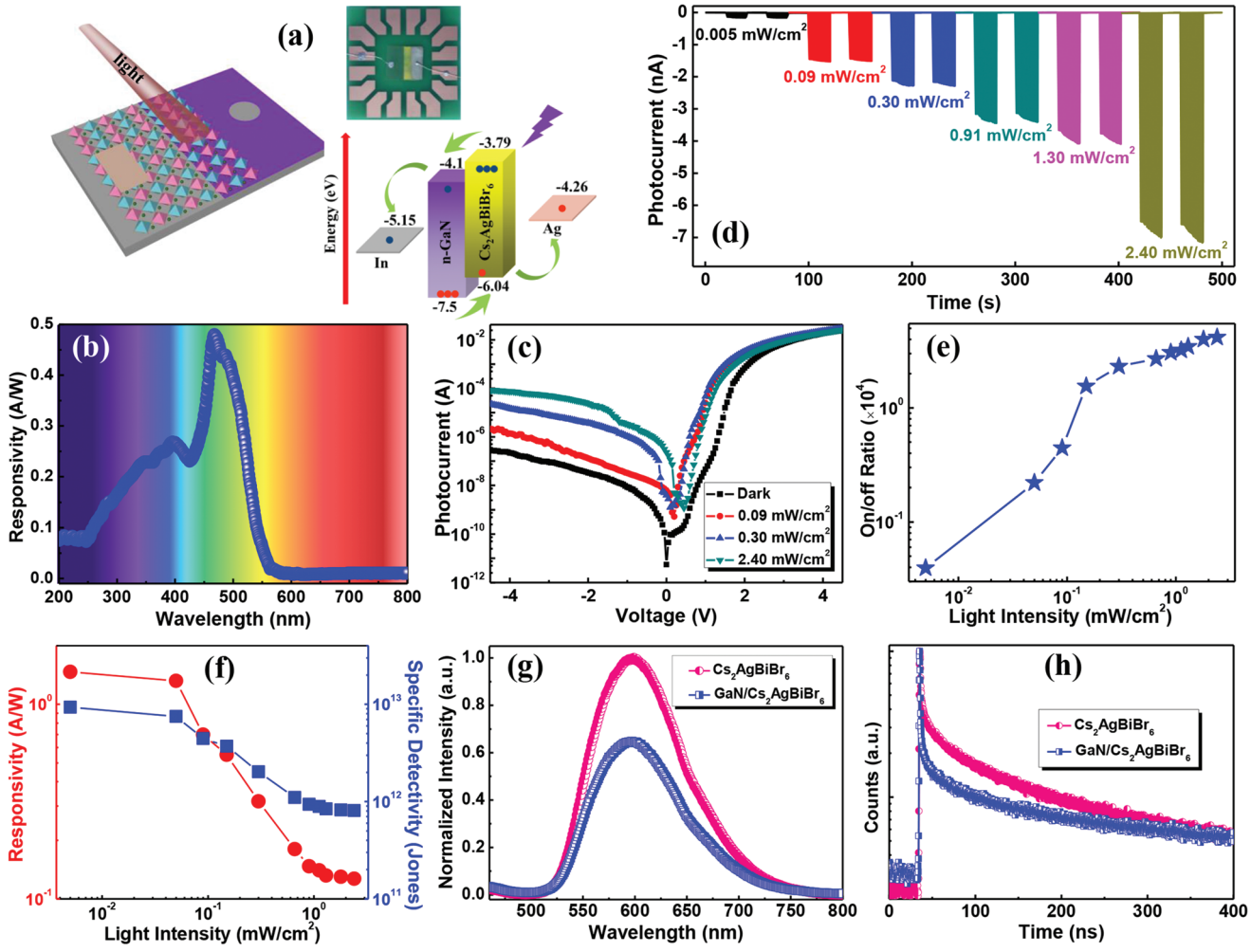

Figure 3. a) Schematic device structure of the $Cs_2AgBiBr_6$/GaN heterojunction photodetector. The right-upper pane is the photograph of the resulting device; the right-bottom pane displays the energy band profile of the heterostructure. b) Spectra response of the photodetector. c) Typical *I*–*V* curves of the heterojunction photodetector tested in dark and under varying light intensity excitation (265 nm). d) Photocurrent response measured under 265 nm light excitation with varying intensity at zero bias. e) Relationship between on/off photocurrent ratio and the light intensity. f) Photoresponsivity and specific detectivity of the photodetector versus light intensity. g) PL spectra, and h) PL decay curves of the $Cs_2AgBiBr_6$ and $Cs_2AgBiBr_6$/GaN hybrid.

To evaluate the selectivity of the heterojunction photodetector to incident light, the spectral response in the range of 200–800 nm was measured at zero bias and displayed in Figure 3b. It can be seen that the photodetector is sensitive to light illumination with wavelength less than 550 nm, and virtually blind to light illumination with longer wavelength. This good spectral selectivity is well in accordance with the absorption curve of $Cs_2AgBiBr_6$ films shown in Figure 1f (green dotted line). Figure 3c shows the typical current–voltage (I–V) characteristics of the photodetector tested in dark and under light excitation (265 nm, 2.40 mW cm^{-2}) from which an excellent rectification characteristic with a rectification ratio over 10^4 (±5 V) in the dark and a significant photoresponse under deep UV light can be observed. Since the Ohmic contact shown in Figure S8 (Supporting Information) has been established between the semiconductors and electrodes, the observed nonlinear rectification behavior are, therefore, considered to arise solely from the heterojunction. Note that a pronounced photovoltaic behavior was observed, enabling the present photodetector to work as a self-powered device without external power supply.

Figure 3d depicts the temporal photocurrent response of the device at varying excitation intensity at zero bias in which both turn-on and turn-off time of incident light were kept at 20 s. Three aspects of this figure were important to note: first, the current can switch reversibly between high and low conductance with high repeatability and stability, indicating a promoted and reproducible photocurrent response. Second, the on/off photocurrent ratio increases monotonously with increasing light excitation intensity, reaching a maximum value of 4.16×10^4 under 2.40 mW cm^{-2} light excitation. Such a high value could ensure the accuracy of the device to detect a weak light signal. Third, with the increase of light illumination intensity, the photocurrent increases gradually and produces a nonlinear dependence, as presented in Figure 3e.

Besides, other key device parameters, photoresponsivity (R) and specific detectivity (D^*), were calculated to evaluate its photoresponse ability quantitatively. R is usually described by the expression of $R = (I_p - I_d)/P_{opt}S$, where I_p is the photocurrent, S is the active area, and P_{opt} represents the intensity of incident light. Figure 3f shows the dependence of R on incident light intensity, and a maximum value of 1.46 A W^{-1} was achieved. In order to avoid the contingency of the experiment, we performed a statistical test on the photoresponsivity of the device at a low power density of 0.005 mW cm^{-2}. It can be observed from Figure S9 (Supporting Information) that the values of R distribute around 1.46 A W^{-1} with a very small fluctuation, confirming the accuracy of the measured data. Besides, we evaluated the D^* of the photodetector using the following relation[43]

$$D^* = \frac{A^{1/2}R}{(2eI_d)^{1/2}} \quad (1)$$

Table 1. Summary of the photodetectors performances.

Device structure	Material structure	Responsivity [A W^{-1}]	D^* [$\times 10^{13}$ Jones]	Ref.
Au/$MAPbI_3$/Au[a)]	single crystal	2.531@5 V	–	[44]
ITO/$MAPbI_3$/ITO	films	3.4@3 V	–	[45]
Au/$MAPbI_3$/Au	nanowire	4.95@1 V	2	[46]
ITO/HTL/$MAPbI_{3-x}Cl_x$/ETL/Al	films	–	10	[47]
Au/polystyrene-$MAPbI_3$/Au	films	0.61@0 V	1.5	[17]
ITO/PET/$MAPbI_3$/Au	films	0.418@0 V	1.22	[48]
ITO/$CsPbBr_3$/ITO	nanosheets	0.64@5 V	–	[49]
Au/$CsPbBr_3$/Au	nanocrystals	0.01@3 V	0.002	[50]
Graphite/$CsPbBr_3$/graphite	microcrystals	2.1@5 V	–	[51]
Au/$CsPbBr_3$/Au	microparticles	0.18@3 V	–	[52]
Ti-Au/$CsPbBr_3$-$CsPb_2Br_5$/Ti-Au	films	0.375@-5 V	0.03	[53]
TiO_2/$MAPbI_3$/Spiro-OMeTAD	films	0.55@-0.1 V	0.1	[54]
ITO/$CsPbBr_3$-ZnO NPs/Ag[b)]	films	0.0115@0 V	–	[55]
Au/$FA_{1-x}Cs_xPbI_3$/Au[c)]	films	5.7@0 V	2.7	[56]
$CsPbX_3$/α-Si radial junction	quantum dots	0.054@0 V	–	[57]
In/GaN-$Cs_2AgBiBr_6$/Ag	films	1.46@0 V	0.94	This work

[a)]$MAPbI_3$: $CH_3NH_3PbI_3$; [b)]NPs: nanoparticles; [c)]$FAPbI_3$: $CH(NH_2)_2PbI_3$.

Based on the equation, the relationship D^* with the light excitation intensity at zero bias was summarized in Figure 3f. One can see that D^* decreases gradually with increasing incident light intensity, and the maximum value was calculated to be 0.94×10^{13} Jones (1 Jones = 1 cm Hz$^{1/2}$ W^{-1}), which are much higher than many reported results based on the lead halide perovskites (**Table 1**). It should be mentioned herein that the values of two parameters share the same decaying trend with increasing light intensity and finally maintain steady levels, which is probably because of the enhanced carrier recombination probability at higher light illumination intensity. In addition, we calculated the value of the linear dynamic range (LDR) of the studied photodetector (Supporting Information).

The response speed is another important characteristic parameter for a photodetector, which reflects its ability to follow a rapidly varying optical signal. In our case, a waveform generator was used to generate the pulsed light with varied frequency, and an oscilloscope was employed to record the change of photocurrent with time. Figure S10 (Supporting Information) illustrates the corresponding experimental setup and the temporal photoresponse properties of the $Cs_2AgBiBr_6$/GaN heterojunction photodetector at various modulating frequencies. It can be seen that the photodetector exhibits a fast switching characteristic and a remarkable reproducibility at all measured frequencies. According to the photocurrent response profile recorded at 50 Hz, the rise time (t_r) (from 10% to 90% of the saturated value) and fall time (t_f) (from 90% to 10% of the peak value) of the device are found to be 3.463 and 8.442 ms, suggesting that the proposed heterojunction photodetector has the ability to follow a fast varying light signal. In addition to the UV light detecting, the photoresponse characteristics of the photodetector to visible light were also examined. Figure S11

(Supporting Information) displays the corresponding *I*–*V* characteristics and time-dependent photoresponse of the photodetector in dark and under 405 and 520 nm light excitation, and obvious photovoltaic effects were also observed.

As mentioned above, the mechanisms of photoresponse for the $Cs_2AgBiBr_6$/GaN heterojunction photodetector may be the efficient charge carrier transfer at the hetero-interface. In order to support this argument, PL spectra of the bare $Cs_2AgBiBr_6$ and $Cs_2AgBiBr_6$/GaN hybrid structure were measured and put together for comparison. As shown in Figure 3g, the integrated PL intensity for the $Cs_2AgBiBr_6$/GaN hybrid structure was quenched by nearly 34% with respect to that of the bare $Cs_2AgBiBr_6$ films. Such a dramatic PL quenching implies that a great proportion of photogenerated carriers may be transferred from the $Cs_2AgBiBr_6$ to the underlying GaN through carrier diffusion because of the relatively large diffusion length of carrier in perovskite.[58,59] Further, we performed the time-resolved PL spectra of two samples to quantify the carrier diffusion length. As shown in Figure 3h, the carrier lifetime of the $Cs_2AgBiBr_6$/GaN hybrid structure decreases substantially, which manifests a faster PL decay channel for the hybrid structure, and is also a direct evidence of electron transfer behavior. Thus, the underlying GaN template can be deemed as the electron-quenching layer. The distribution of photogenerated electrons $n(x, t)$ in the $Cs_2AgBiBr_6$ films can be described by the following one-dimensional (1D) diffusion model

$$\frac{\partial n(x,t)}{\partial t} = D\frac{\partial^2 n(x,t)}{\partial^2 t} - n(x,t)\,k(t) \tag{2}$$

where D is the diffusion coefficient of electrons, and $k(t)$ represents the radiative decay rate of $Cs_2AgBiBr_6$ films. Herein, a hypothesis was made that the photogenerated electrons will be quenched as they reach the $Cs_2AgBiBr_6$/GaN interface. Therefore, we can use the boundary conditions $n(L, t) = 0$ to analyze the above equation, where L is the thickness of $Cs_2AgBiBr_6$ films, and $x = 0$ represents the $Cs_2AgBiBr_6$/GaN interface. The characteristic diffusion length (L_D) of electrons was then determined from $L_D = \sqrt{D\,\tau}$, where τ is the recombination lifetime in the absence of the electron quencher (GaN). Finally, the value of L_D was estimated to be 139 nm, comparable with the data reported in popular $CH_3NH_3PbI_3$ materials.[23,58,60] Such a large electron diffusion length, on the premise of a light absorption depth of 100–200 nm, implies that the photogenerated electrons have the ability and probability to travel through the $Cs_2AgBiBr_6$ films to the underlying GaN layer; thus, the proposed planar $Cs_2AgBiBr_6$/GaN heterojunction photodetector are expected to operate well. Of course, more work should be done for achieving an even larger L_D by optimizing the microstructures of the $Cs_2AgBiBr_6$ films.

As is well known, the operation stability of perovskite-based optoelectronic devices has always been a challenging issue.[61,62] From application point of view, developing stable and environment-friendly photodetectors compatibility for practical applications is highly desired. In theory, after a continuous running for a long period, increased heating effect in the photodetectors would be generated, and the temperature of the device chip will be increased, which would inevitably induce a rapid proliferation of structural defects. Thus, the photogenerated charge carriers could be quickly captured by these undesirable trap states. As a result, the long-term operation stability and thermal stability of the perovskite photodetectors would face the challenges. To examine the long-term stability of the unencapsulated photodetector, the dependence of photocurrent on running time was investigated at air ambient condition (293 K, 35–50% humidity), where a light excitation intensity of 0.30 mW cm^{-2} and a zero bias were fixed and the photocurrent was monitored in real time. As displayed in **Figure 4**b (green line), the photocurrent of the device exhibits an ultrastable behavior after operation continuously for 10 h, without any drop over the running time, and the corresponding temporal photoresponse curves of the device before aging and after operation for 10 h were presented in Figure 4a and c (green line), respectively. The results indicate that the proposed photodetector has excellent operation stability, and also suggest that the lead-free double perovskite $Cs_2AgBiBr_6$ films can serve as an effective and reliable light absorber for photodetector application. In real life, the functional photodetectors have to work in the open air with inconsistent conditions, such as a harsh environment with a high temperature. Therefore, we further conducted the temperature-dependent aging tests to evaluate the temperature resistance of the heterojunction photodetector. For measurements, the unencapsulated photodetector was mounted on a heating plate and heated externally to three investigated temperature points (333, 353, and 373 K) with other measurement conditions unchanged for comparison. From the other three lines plotted in Figure 4b, a regular evolution of the photocurrent could be observed, which decays gradually with increasing working temperature. Specifically, the photocurrent decreases to 83.3% (333 K), 75.0% (353 K), and 70.9% (373 K) of the original value after 10 h running time, respectively. Despite this, the device stability in present case is still better than that in previous reports.[63,64] Herein, we attributed the reduction of photocurrent to the increased structural defects by the heating effect by which the photogenerated carriers were trapped quickly. The above experiments indicate a remarkable temperature resistance of the heterojunction photodetector, and also a rational device design with an all-inorganic configuration compatible for practical applications under harsh conditions.

An additional and very important observation is that the photocurrent of the proposed photodetector is recoverable if the heating effect is eliminated by the cooling process. Figure 4c and d display the temporal photoresponse curves of the unencapsulated device after aging, and after cooled down to room-temperature (RT) naturally, respectively. On the one hand, the reduced photocurrent level after operation for 10 h (Figure 4c) and the increased decay magnitude at higher temperatures are consistent with the above discussions. On the other hand, after the heated device was cooled down to RT naturally, the corresponding photoresponse increases substantially, demonstrating the nearly identical values as compared with the measured data before aging test (333, 353 K). Only for the aging test at 373 K, a residual photocurrent decay of about 15% was observed. Therefore, a conclusion could be made that the photocurrent degradation at high temperature is recoverable, but it could not be completely recovered above a certain critical aging temperature, which is well consistent with the experimental results in thermal cycling PL measurements shown in Figure 2g–i.

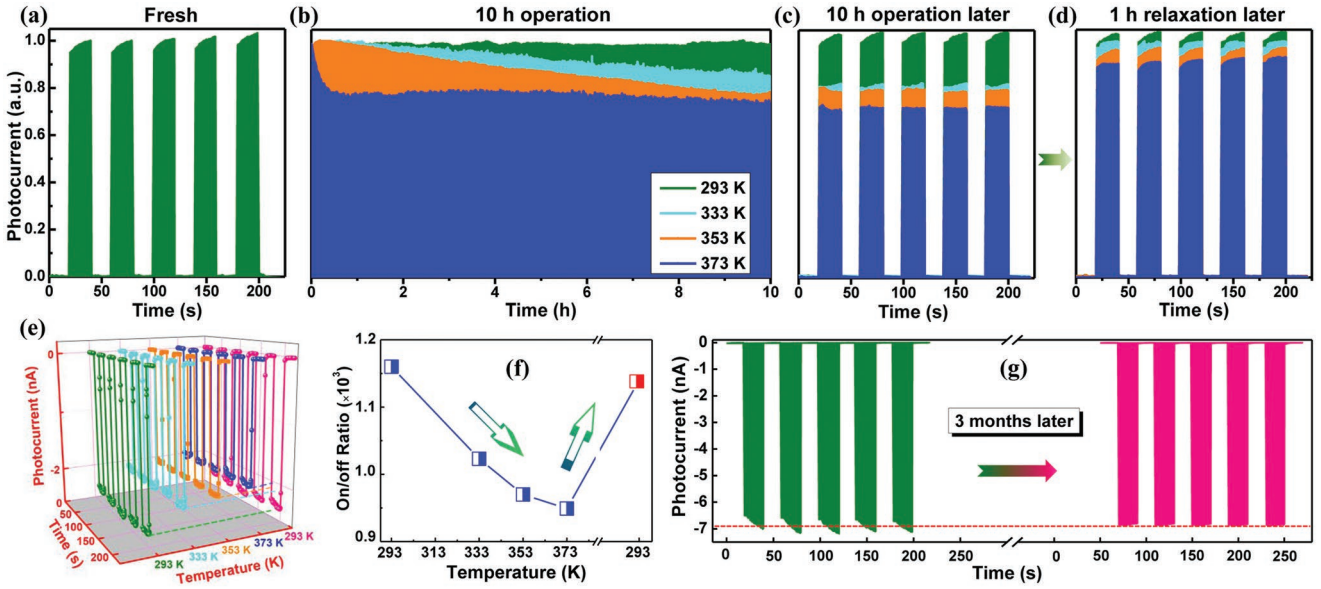

Figure 4. a) Temporal photoresponse curves of the unencapsulated device before aging. b) Normalized photocurrent of the unencapsulated heterojunction photodetector versus running time at 293 K (green line), 333 K (cyan line), 353 K (orange line), and 373 K (blue line), respectively (265 nm, 0.30 mW cm^{-2}). Temporal photoresponse curves of the unencapsulated device c) after aging, and d) after cooled down to RT naturally. e) Temperature-dependent photocurrent–time curves at zero bias at constant light illumination (265 nm, 0.30 mW cm^{-2}). f) One thermal cycling measurement of the heterojunction photodetector showing its variation on the on/off photocurrent ratio at different temperatures. g) Stability of the unencapsulated device after 3-month storage in the open air. The last five cycles correspond to the photoresponse after storage in air for three months (20 °C, 35–50% humidity).

For a better understanding on the temperature resistance of the photodetector, temperature-dependent photocurrent–time curves of the device were put together for comparison. As shown in Figure 4e, some distinct but regular changing trends were revealed, and the photocurrent decreases monotonously with the increasing temperature under the same measurement conditions. As such temperature levels are not sufficient to induce chemical reaction or phase transition in the $Cs_2AgBiBr_6$ products (Figure S12, Supporting Information), we herein propose that the decreasing photocurrent is presumably because of the increased trap states in the $Cs_2AgBiBr_6$ absorber at high temperature by which the photogenerated carriers are quickly trapped. Of course, there is also an indisputable fact that an increased charge carrier density in the $Cs_2AgBiBr_6$ films would be induced upon high temperature, lowering the effective energy barrier height and allowing easier carrier transport to some extent, which is beneficial for the enhancement in conductivity. Therefore, one can conclude that there exists a competitive relationship between the above two factors. Obviously, the photogenerated carrier trapping process at high temperature dominates over the contribution of carrier density increase at all measured temperature points. Based on the obtained data from temperature-dependent photocurrent–time curves, the on/off photocurrent ratios of the device at four temperature points (RT, 333, 353, and 373 K) were calculated and summarized in Figure 4f, and an obvious weakening trend can be distinguished. At 333 K, the on/off photocurrent ratio decreases by 11.81%, and at 373 K, 81.81% of the initial value remains. Although a reduced on/off photocurrent ratio was induced as the heterojunction photodetector was operated at high temperature, a significant progress on operation stability makes practical applications of such photodetectors a real possibility. More interestingly and excitingly, the on/off photocurrent ratio of the device could nearly recover to its initial level after the working device was naturally cooled down to RT (extracted from the pink line in Figure 4e). The above observations indicate the stable and reproducible characteristics of the proposed heterojunction photodetector and also its good temperature resistance, promoting the existing applications and suggesting other potentials. Moreover, the present device can keep nearly the identical photocurrent and work properly even after 3-month storage in the open air, and the test conditions are consistent (265 nm, 2.4 mW cm^{-2}), as presented in Figure 4g, without any encapsulation and protection, greatly superior to the performance of $CH_3NH_3PbX_3$-based photodetectors with a poor stability. Figure S13 (Supporting Information) displays the XRD results of the $Cs_2AgBiBr_6$ films before and after 3-month storage. One can see that all the diffraction peaks correspond to the cubic $Cs_2AgBiBr_6$ without the appearance of other parasitic diffraction signals, indicating that the phase purity of $Cs_2AgBiBr_6$ films was retained after 3-month duration, in other words, their remarkable intrinsic/environmental stability. The remarkable material stability together with the good device performance suggest the $Cs_2AgBiBr_6$ films are effective and reliable building blocks for photodetector applications, and will render the present environment-friendly photodetectors potentially useful for the assembly of optoelectronic system in future.

Image sensors are widely used in digital camera, industry, and defense.[65,66] Because of the remarkable device performance and facility of the photodetector fabrication, the detector image of the heterojunction photodetector was further evaluated by

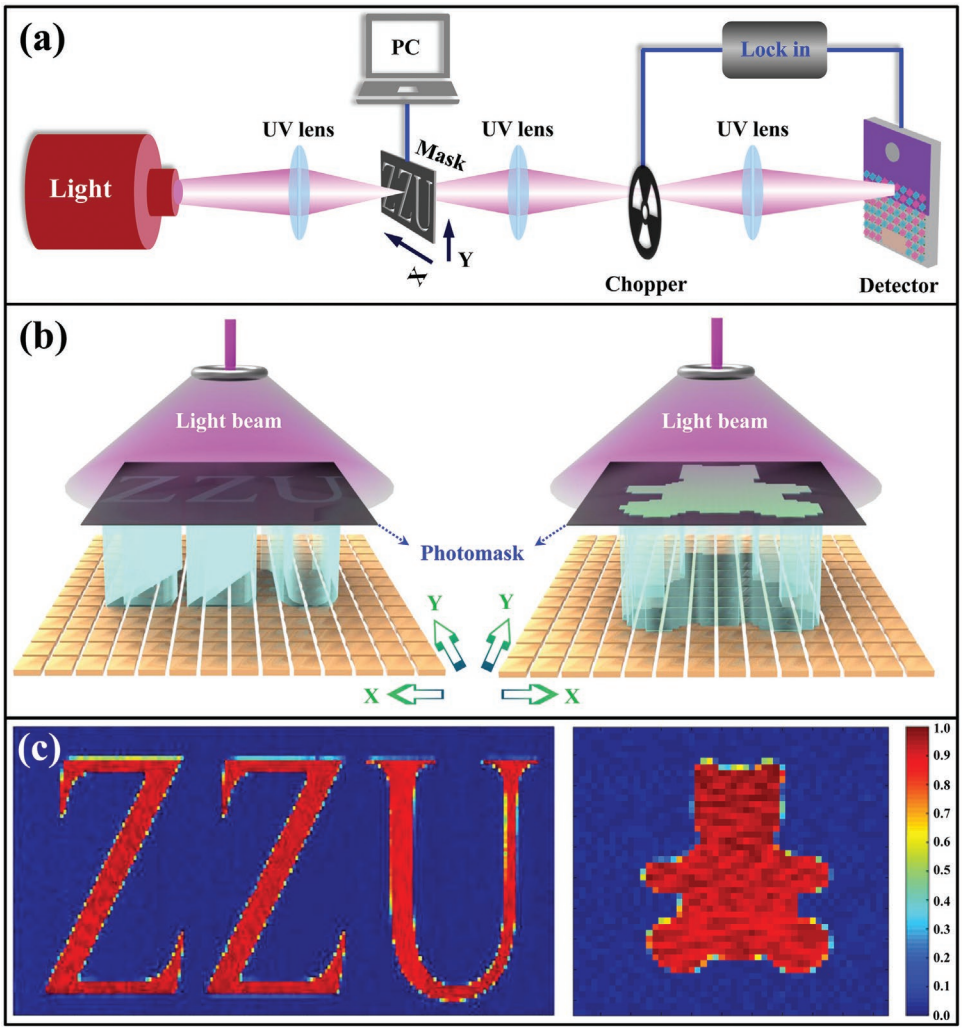

Figure 5. a) Schematic diagram of the imaging system using the heterojunction photodetector as the sensing pixel operated at zero bias. b) Mechanism of the projection imaging process. c) Imaging results of Zhengzhou University logo "ZZU" and a symbol of a bear.

employing the device as sensing pixels. The schematic illustration of the measurement system made up of a patterned photomask, a light source, and a heterojunction photodetector was displayed in **Figure 5**a, where the photodetector was used as a point-like detector to extract the light signals, and the photomask with hollow patterns (ZZU, a symbol of a bear) was mounted on a computer-controlled 2D translation stage that can be continuously moved along a meandering path through the focus of the light beam. The photocurrent signal generated by the excitation of light beam passing through the hollow patterns was collected by a lock-in amplifier controlled by the computer for synchronization with the 2D translation stage. By using this measurement system, solar-blind imaging based on single-crystalline diamond photodetectors has been reported by our group recently.[67] Figure 5b illustrates the projection imaging process, and the optical imaging patterns can be obtained by using the bright and dark contrast under the light illumination and the position coordinates, as sensed by the photodetector placed under the photomask. Figure 5c presents two typical imaging results including Zhengzhou University logo "ZZU" and a symbol of a bear with sharp boundaries, which were obtained by converting the photocurrent value to the grayscale number. One can see that two patterns were clearly resolved and well consistent with the object in shape, implying the high fidelity characteristics of the imaging system and the reliable imaging function of the proposed sensor device. Note that this is the first report on imaging applications of lead-free perovskite photodetectors to the best of our knowledge, making the results original and beneficial to progress toward a practical image sensor.

3. Conclusions

In conclusion, we have successfully demonstrated a self-powered photodetector by employing solution-processed lead-free double perovskites $Cs_2AgBiBr_6$ films as the light absorber. Because of the high material integrity of $Cs_2AgBiBr_6$ films and efficient interfacial charge transfer effect, the proposed photodetector demonstrates an on/off ratio of 4.16×10^4, a

high photoresponsivity of 1.46 A W^{-1}, and a specific detectivity of 0.94×10^{13} Jones. More importantly, the unencapsulated photodetector possesses remarkable operation stability against water and oxygen degradation (air ambient, 35–50% humidity). Even at a high working temperature of 373 K for 10 h continuous running and/or after a 3-month storage in the open air, the device can function properly and its photodetection ability can be almost maintained, indicating a good temperature resistance and a desired compatibility for practical applications under harsh conditions. Moreover, the proposed photodetector has been employed as the sensing pixels in an imaging system, and high-resolution imaging patterns were obtained, which is the first studyon imaging applications of lead-free perovskite photodetectors. The results demonstrated here highlight the great potential of lead-free double perovskite $Cs_2AgBiBr_6$ as environment-friendly alternatives for high-efficiency and stable photodetectors that can be employed in optical imaging.

4. Experimental Section

Preparation of $Cs_2AgBiBr_6$ Films: In this work, the preparation process began with a commercially available n-GaN/Al_2O_3 substrate, and it was cleaned ultrasonically with acetone, ethanol, and deionized water for 10 min, respectively. Then the substrate was treated with Ar gas plasma for 10 min in order to improve the substrate wettability. In this case, the lead-free metal halide double perovskites $Cs_2AgBiBr_6$ films were prepared through the one-step spin-coating method. First, a mixture of AgBr (99.9%), $BiBr_3$ (98%), and CsBr (99.9%) was dissolved in 1 mL of dimethyl sulfoxide to form a 0.5 mol L^{-1} precursor solution. Then 100 µL of the precursor solution was spin-coated on the GaN/Al_2O_3 template with 500 rpm for 10 s (low-speed spinning) and then 2000 rpm for 30 s (high-speed spinning). In order to remove the solvent quickly and obtain a good coverage, the resulting sample after spin-coating was left under vacuum and kept undisturbed for 30 min. Following that, the sample was placed in a tube furnace (OTF-1200X) under ambient conditions and annealed at 285 °C for 5 min to form the $Cs_2AgBiBr_6$ perovskites.

Fabrication of Devices: For device preparation, In electrode (≈80 nm) on GaN and Ag electrode (≈50 nm) on the $Cs_2AgBiBr_6$ films were deposited by e-beam evaporation. A shadow mask with diameter of 2 mm was used to pattern electrode on the films. The heterojunction was established at the area where perovskite and GaN are overlapped, with a width of 2 mm and length of 1 cm. The active area of the device was the light spot area, and its diameter was 60 µm.

Characterization of Materials and Devices: The morphology of the produced $Cs_2AgBiBr_6$ perovskites were measured by field-emission SEM (Jeol-7500F, 15 keV). The microstructures of the sample was analyzed by a high-resolution TEM with a JEM-3010 electron microscope. XRD was performed using Panalytical X'Pert Pro. The EDS attached to the SEM was used to analyze the element composition. The chemical composition and bond states were investigated by XPS (SPECS XR50). The absorption spectra was measured using a Shimadzu UV-3150 spectrophotometer. The PL spectra were recorded using a spectrofluorometer (Horiba; Fluorolog-3), and the transient PL measurement was conducted using a pulsed NanoLED (Horiba; 371 nm). The electrical property of the GaN layer was measured by Hall effect measurements (ACCENT HL5500PC, UK). Thermogravimetric analysis (TGA) was tested under N_2 environment with a NetzschTG209F3 TGA system (heating rate, 5 °C min^{-1}). The electrical and optoelectrical tests were performed by using a testing system that includes light sources, a monochromator, a digital SourceMeter (Keithley 2636B), optical chopper (SRS, SR540), and an oscilloscope (Tektronix, DPO2012B) in air.

Theoretical Calculations: The first-principles calculation was performed through plane-wave pseudopotential approach within density functional theory as administered in the Vienna ab initio simulation package. The electron–ion interaction was described by the projected augmented wave pseudopotentials with $5s^25p^66s$ for Cs, $6s^26p^3$ for Bi, $4d^{10}5s$ for Ag, and $4s^24p^5$ for Br as the valence electron. The exchange-correlation functional was established by the generalized gradient approximation, which was formulated by Ernzerhof–Burke–Perdew. A kinetic energy cutoff (400 eV) and *k*-point meshes (spacings, $2\pi \times 0.03$ $Å^{-1}$) were used for the expansion of wave function and integration of electronic Brillouin zone. By the total energy minimization with the residual forces on the atoms converged to below 0.01 eV $Å^{-1}$, the internal coordinate, lattice parameter, and other equilibrium structural parameters were optimized. The Heyd–Scuseria–Ernzerhof hybrid functional method including spin-orbit coupling effect was employed to obtain reliable band gaps. To synthesize the stable $Cs_2AgBiBr_6$ films in material growth, a certain region of chemical potentials under thermal equilibrium condition need to be satisfied

$$2\Delta\mu_{Cs} + \Delta\mu_{Ag} + \Delta\mu_{Bi} + 6\Delta\mu_{Br} = \Delta H_{Cs_2AgBiBr_6} \quad (3)$$

$$\Delta\mu_i \le 0 \quad (i = \mathrm{Cs,Ag,Bi,Br}) \quad (4)$$

$$h_j\Delta\mu_{Cs} + k_j\Delta\mu_{Ag} + n_j\Delta\mu_{Bi} + m_j\Delta\mu_{Br} \le \Delta H_{Cs_{h_j}Ag_{k_j}Bi_{n_j}Br_{m_j}}, \quad j = 1\cdots Z \quad (5)$$

Equation (3) is for thermodynamic equilibrium, Equation (4) is to prevent the atomic species from precipitating to elemental phases, and Equation (5) is to avoid the formation of any secondary competing phase. The stability diagram is obtained, when the thermal equilibrium condition (formula 3–5) are satisfied at the same time. Under these constrains, $\Delta\mu_{Cs}$, $\Delta\mu_{Ag}$, and $\Delta\mu_{Bi}$, that stabilize $Cs_2AgBiBr_6$ are bound in a polyhedron in 3D space. The 2D slices of the 3D stable region taken at selected $\Delta\mu_{Bi}$ are shown in Figure S6 (Supporting Information).

Supporting Information

Supporting Information is available from the Wiley Online Library or from the author.

Acknowledgements

This work was supported by the National Natural Science Foundation of China (Nos. 11774318, 11604302, 61176044, and 11504331), the China Postdoctoral Science Foundation (2017T100535), the Key Scientific Research Projects of Higher Education in Henan Province (18A140007), the Support Program for Scientific and Technological Innovation Talents of Higher Education in Henan Province (19HASTIT017), and the Outstanding Young Talent Research Fund of Zhengzhou University (1521317001).

Conflict of Interest

The authors declare no conflict of interest.

Keywords

$Cs_2AgBiBr_6$, imaging, lead-free, photodetectors, stability

Received: January 27, 2019
Revised: February 24, 2019
Published online:

[1] M. M. Lee, J. Teuscher, T. Miyasaka, T. N. Murakami, H. J. Snaith, *Science* **2012**, *338*, 643.
[2] Q. F. Dong, Y. J. Fang, Y. C. Shao, P. Mulligan, J. Qiu, L. Cao, J. S. Huang, *Science* **2015**, *347*, 967.
[3] L. Protesescu, S. Yakunin, M. I. Bodnarchuk, F. Krieg, R. Caputo, C. H. Hendon, R. X. Yang, A. Walsh, M. V. Kovalenko, *Nano Lett.* **2015**, *15*, 3692.
[4] Z. Shi, S. Li, Y. Li, H. Ji, X. Li, D. Wu, T. Xu, Y. Chen, Y. Tian, Y. Zhang, C. Shan, G. Du, *ACS Nano* **2018**, *12*, 1462.
[5] M. Y. Leng, Z. W. Chen, Y. Yang, Z. Li, K. Zeng, K. H. Li, G. D. Niu, Y. He, Q. C. Zhou, J. Tang, *Angew. Chem., Int. Ed.* **2016**, *55*, 15012.
[6] W. Hu, W. Huang, S. Yang, X. Wang, Z. Jiang, X. Zhu, H. Zhou, H. Liu, Q. Zhang, X. J. Zhuang, J. L. Yang, D. H. Kim, A. L. Pan, *Adv. Mater.* **2017**, *29*, 1703256.
[7] Y. Bekenstein, B. A. Koscher, S. W. Eaton, P. D. Yang, A. P. Alivisatos, *J. Am. Chem. Soc.* **2015**, *137*, 16008.
[8] S. Yakunin, L. Protesescu, F. Krieg, M. I. Bodnarchuk, G. Nedelcu, M. Humer, G. D. Luca, M. Fiebig, W. Heiss, M. V. Kovalenko, *Nat. Commun.* **2015**, *6*, 8056.
[9] Z. Shi, Y. Li, S. Li, X. Li, D. Wu, T. Xu, Y. Tian, Y. Chen, Y. Zhang, B. Zhang, C. Shan, G. Du, *Adv. Funct. Mater.* **2018**, *28*, 1707031.
[10] Z. X. Zhang, L. H. Zeng, X. W. Tong, Y. Gao, C. Xie, Y. H. Tsang, L. B. Luo, Y. C. Wu, *J. Phys. Chem. Lett.* **2018**, *9*, 1185.
[11] A. Miyata, A. Mitioglu, P. Plochocka, O. Portugall, J. T. Wang, S. D. Stranks, H. J. Snaith, R. J. Nicholas, *Nat. Phys.* **2015**, *11*, 582.
[12] J. C. Zhou, J. Huang, *Adv. Sci.* **2018**, *5*, 1700256.
[13] Y. C. Liu, J. K. Sun, Z. Yang, D. Yang, X. D. Ren, H. Xu, Z. Yang, S. Z. Liu, *Adv. Opt. Mater.* **2016**, *4*, 1829.
[14] Z. Zheng, F. Zhuge, Y. Wang, J. Zhang, L. Gan, X. Zhou, H. Li, T. Y. Zhai, *Adv. Funct. Mater.* **2017**, *27*, 1703115.
[15] W. Deng, L. M. Huang, X. Z. Xu, X. J. Zhang, X. C. Jin, S. T. Lee, J. S. Jie, *Nano Lett.* **2017**, *17*, 2482.
[16] Y. Li, Z. F. Shi, L. Z. Lei, Z. Z. Ma, F. Zhang, S. Li, D. Wu, T. Xu, X. Li, C. X. Shan, G. T. Du, *ACS Photonics* **2018**, *5*, 2524.
[17] R. Saraf, V. Maheshwari, *ACS Appl. Mater. Interfaces* **2018**, *10*, 21066.
[18] F. Bai, J. J. Qi, F. Li, Y. Y. Fang, W. P. Han, H. L. Wu, Y. Zhang, *Adv. Mater. Interfaces* **2018**, *5*, 1701275.
[19] H. Zhou, J. Mei, M. N. Xue, Z. H. Song, H. Wang, *J. Phys. Chem. C* **2017**, *121*, 21541.
[20] F. Yuan, J. Xi, H. Dong, K. Xi, W. W. Zhang, C. Ran, B. Jia, X. Hou, A. K. Y. Jen, Z. X. Wu, *Physica Status Solidi RRL* **2018**, *12*, 1800090.
[21] Z. R. Zhao, F. Gu, Y. L. Li, W. H. Sun, S. Y. Ye, H. X. Rao, Z. W. Liu, Z. Q. Bian, C. H. Huang, *Adv. Sci.* **2017**, *4*, 1700204.
[22] E. T. McClure, M. R. Ball, W. Windl, P. M. Woodward, *Chem. Mater.* **2016**, *28*, 1348.
[23] W. Ning, F. Wang, B. Wu, J. Lu, Z. Yan, X. Liu, Y. Tao, J. M. Liu, W. Huang, M. Fahlman, L. Hultman, T. C. Sum, F. Gao, *Adv. Mater.* **2018**, *30*, 1706246.
[24] A. H. Slavney, T. Hu, A. M. Lindenberg, H. I. Karunadasa, *J. Am. Chem. Soc.* **2016**, *138*, 2138.
[25] G. Volonakis, A. A. Haghighirad, R. L. Milot, W. H. Sio, M. R. Filip, B. Wenger, M. B. Johnston, L. M. Herz, H. J. Snaith, F. Giustino, *J. Phys. Chem. Lett.* **2017**, *8*, 772.
[26] X. G. Zhao, D. W. Yang, Y. H. Sun, T. S. Li, L. J. Zhang, L. P. Yu, A. Zunger, *J. Am. Chem. Soc.* **2017**, *139*, 6718.
[27] L. Z. Lei, Z. F. Shi, Y. Li, Z. Z. Ma, F. Zhang, T. T. Xu, Y. T. Tian, D. Wu, X. J. Li, G. T. Du, *J. Mater. Chem. C* **2018**, *6*, 7982.
[28] X. G. Zhao, J. H. Yang, Y. H. Fu, D. W. Yang, Q. L. Xu, L. P. Yu, S. H. Wei, L. J. Zhang, *J. Am. Chem. Soc.* **2017**, *139*, 2630.
[29] G. Volonakis, A. A. Haghighirad, H. J. Snaith, F. Giustino, *J. Phys. Chem. Lett.* **2017**, *8*, 3917.
[30] Z. W. Xiao, K. Z. Du, W. W. Meng, J. B. Wang, D. B. Mitzi, Y. F. Yan, *J. Am. Chem. Soc.* **2017**, *139*, 6054.
[31] W. Pan, H. Wu, J. Luo, Z. Deng, C. Ge, C. Chen, X. Jiang, W. J. Yin, G. Niu, L. Zhu, L. Yin, Y. Zhou, Q. Xie, X. Ke, M. Sui, J. Tang, *Nat. Photonics* **2017**, *11*, 726.
[32] B. Yang, J. Chen, S. Yang, F. Hong, L. Sun, P. Han, T. Pullerits, W. Deng, K. L. Han, *Angew. Chem., Int. Ed.* **2018**, *57*, 5359.
[33] C. C. Wu, Q. H. Zhang, Y. Liu, W. Luo, X. Guo, Z. R. Huang, H. Ting, W. H. Sun, X. R. Zhong, S. Y. Wei, S. F. Wang, Z. J. Chen, L. X. Xiao, *Adv. Sci.* **2018**, *5*, 1700759.
[34] L. Zhou, Y. F. Xu, B. X. Chen, D. B. Kuang, C. Y. Su, *Small* **2018**, *14*, 1703762.
[35] E. Greul, M. L. Petrus, A. Binek, P. Docampo, T. Bein, *J. Mater. Chem. A* **2017**, *5*, 19972.
[36] E. M. Hutter, M. C. Gelvez-Rueda, D. Bartesaghi, F. C. Grozema, T. J. Savenije, *ACS Omega* **2018**, *3*, 11655.
[37] J. A. Steele, P. Puech, M. Keshavarz, R. Yang, S. Banerjee, E. Debraye, C. W. Kim, H. F. Yuan, N. H. Heo, J. Vanacken, A. Walsh, J. Hofkens, M. B. J. Roeffaers, *ACS Nano* **2018**, *12*, 8081.
[38] W. J. Yin, T. T. Shi, Y. F. Yan, *Appl. Phys. Lett.* **2014**, *104*, 063903.
[39] W. M. Ming, S. Y. Chen, M. H. Du, *J. Mater. Chem. A* **2016**, *4*, 16975.
[40] Y. Zhang, J. Du, X. H. Wu, G. Q. Zhang, Y. L. Chu, D. P. Liu, Y. X. Zhao, Z. Q. Liang, J. Huang, *ACS Appl. Mater. Interfaces* **2015**, *7*, 21634.
[41] W. Tian, H. P. Zhou, L. Li, *Small* **2017**, *13*, 1702017.
[42] M. Y. Leng, Y. Yang, K. Zeng, Z. W. Chen, Z. F. Tan, S. R. Li, J. H. Li, B. Xu, D. B. Li, M. P. Hautzinger, Y. P. Fu, T. Y. Zhai, L. Xu, G. D. Niu, J. Tang, *Adv. Funct. Mater.* **2018**, *28*, 1704446.
[43] T. Gao, Q. Zhang, J. N. Chen, X. Xiong, T. Y. Zhai, *Adv. Opt. Mater.* **2017**, *5*, 1700206.
[44] J. X. Ding, S. J. Du, Y. Zhao, X. J. Zhang, Z. Y. Zuo, H. Z. Cui, X. Y. Zhan, Y. J. Gu, H. Q. Sun, *J. Mater. Sci.* **2017**, *52*, 276.
[45] X. Hu, X. Zhang, L. Liang, J. Bao, S. Li, W. Yang, Y. Xie, *Adv. Funct. Mater.* **2014**, *24*, 7373.
[46] L. Gao, K. Zeng, J. S. Guo, C. Ge, J. Du, Y. Zhao, C. Chen, H. Deng, Y. S. He, H. S. Song, G. D. Ni, J. Tang, *Nano Lett.* **2016**, *16*, 7446.
[47] L. Dou, Y. Yang, J. You, Z. Hong, W.-H. Chang, G. Li, Y. Tang, *Nat. Commun.* **2014**, *5*, 5404.
[48] S. F. Leung, K. T. Ho, P. K. Kung, V. K. S. Hsiao, H. N. Alshareef, Z. L. Wang, J. H. He, *Adv. Mater.* **2018**, *30*, 1704611.
[49] J. Z. Song, L. M. Xu, J. H. Li, J. Xue, Y. H. Dong, X. M. Li, H. B. Zeng, *Adv. Mater.* **2016**, *28*, 4861.
[50] Y. H. Dong, Y. Gu, Y. S. Zou, J. Z. Song, L. M. Xu, J. H. Li, J. Xue, X. M. Li, H. B. Zeng, *Small* **2016**, *12*, 5622.
[51] F. Cao, D. J. Yu, X. M. Li, Y. Zhu, Z. G. Sun, Y. L. Shen, Y. Wu, Y. Wei, H. B. Zeng, *J. Mater. Chem. C* **2017**, *5*, 7441.
[52] X. M. Li, D. Yu, F. Cao, Y. Gu, Y. Wei, Y. Wu, J. Z. Song, H. B. Zeng, *Adv. Funct. Mater.* **2016**, *26*, 5903.
[53] G. Tong, H. Li, D. Li, Z. Zhu, E. Xu, G. Li, L. Yu, J. Xu, Y. Jiang, *Small* **2018**, *14*, 1702523.
[54] G. Q. Tong, X. S. Geng, Y. Q. Yu, L. W. Yu, J. Xu, Y. Jiang, Y. Sheng, Y. Shi, K. J. Chen, *Adv. Funct. Mater.* **2017**, *7*, 18224.
[55] C. L. Li, C. Han, Y. B. Zhang, Z. G. Zang, M. Wang, X. S. Tang, *Sol. Energy Mater. Sol. Cells* **2017**, *172*, 341.
[56] F. X. Liang, J. Z. Wang, Z. X. Zhang, Y. Y. Wang, Y. Gao, L. B. Luo, *Adv. Opt. Mater.* **2017**, *5*, 1700654.
[57] J. W. Lu, X. X. Sheng, G. Q. Tong, Z. W. Yu, X. L. Sun, L. W. Yu, X. X. Xu, J. Z. Wang, J. Xu, Y. Shi, K. J. Chen, *Adv. Mater.* **2017**, *29*, 1700400.
[58] S. D. Stranks, G. E. Eperon, G. Grancini, C. Menelaou, M. J. P. Alcocer, T. Leijtens, L. M. Herz, A. Petrozza, H. J. Snaith, *Science* **2013**, *342*, 341.
[59] G. C. Xing, N. Mathews, S. Sun, S. S. Lim, Y. M. Lam, M. Grätzel, S. Mhaisalkar, T. C. Sum, *Science* **2013**, *342*, 344.

[60] M. Chen, M. G. Ju, A. D. Carl, Y. X. Zong, R. L. Grimm, J. J. Gu, X. C. Zeng, Y. Y. Zhu, N. P. Padture, *Joule* **2018**, *2*, 558.
[61] Z. F. Shi, Y. Li, Y. T. Zhang, Y. S. Chen, X. J. Li, D. Wu, T. Xu, C. X. Shan, G. T. Du, *Nano Lett.* **2017**, *17*, 313.
[62] F. Chen, C. X. Xu, Q. Y. Xu, Z. Zhu, F. F. Qin, A. G. Manohari, Y. Z. Zhu, *J. Mater. Chem. C* **2017**, *5*, 9238.
[63] K. Aitola, K. Domanski, J. P. C. Baena, K. Sveinbjörnsson, M. Saliba, A. Abate, M. Grätzel, E. Kauppinen, E. M. J. Johansson, W. Tress, A. Hagfeldt, G. Boschloo, *Adv. Mater.* **2017**, *29*, 1606398.
[64] Y. Li, Z. Shi, S. Li, L. Lei, H. Ji, D. Wu, T. Xu, Y. Tian, X. Li, *J. Mater. Chem. C* **2017**, *5*, 8355.
[65] L. D. Li, Z. Lou, G. Z. Shen, *Adv. Funct. Mater.* **2018**, *28*, 1705389.
[66] W. Deng, X. J. Zhang, L. M. Huang, X. Z. Xu, L. Wang, J. C. Wang, Q. X. Shang, S. T. Lee, J. S. Jie, *Adv. Mater.* **2016**, *28*, 2201.
[67] C. N. Lin, Y. J. Lu, X. Yang, Y. Z. Tian, C. J. Gao, J. L. Sun, L. Dong, F. Zhang, W. D. Hu, C. X. Shan, *Adv. Opt. Mater.* **2018**, *6*, 1800068.

